RSC Advances

PAPER

View Article Online
View Journal | View Issue

Check for updates

Cite this: *RSC Adv.*, 2021, **11**, 16698

Novel biodegradable low-κ dielectric nanomaterials from natural polyphenols†

Sujoy Saha, Sheeba Dawood, Pravalika Butreddy, Gayani Pathiraja and Hemali Rathnayake *

Biodegradable natural polymers and macromolecules for transient electronics have great potential to reduce the environmental footprint and provide opportunities to create emerging and environmentally sustainable technologies. Creating complex electronic devices from biodegradable materials requires exploring their chemical design pathways to use them as substrates, dielectric insulators, conductors, and semiconductors. While most research exploration has been conducted using natural polymers as substrates for electronic devices, a very few natural polymers have been explored as dielectric insulators, but they possess high dielectric constants. Herein, for the first time, we have demonstrated a natural polyphenol-based nanomaterial, derived from tannic acid as a low-κ dielectric material by introducing a highly nanoporous framework with a silsesquioxane core structure. Utilizing natural tannic acid, porous "raspberry-like" nanoparticles (TA-NPs) are prepared by a sol–gel polymerization method, starting from reactive silane unit-functionalized tannic acid. Particle composition, thermal stability, porosity distribution, and morphology are analyzed, confirming the mesoporous nature of the nanoparticles with an average pore diameter ranging from 19 to 23 nm, pore volume of 0.032 $cm^3\ g^{-1}$ and thermal stability up to 350 °C. The dielectric properties of the TA-NPs, silane functionalized tannic acid precursor, and tannic acid are evaluated and compared by fabricating thin film capacitors under ambient conditions. The dielectric constants (κ) are found to be 2.98, 2.84, and 2.69 ($\pm$0.02) for tannic acid, tannic acid-silane, and TA-NPs, respectively. The unique chemical design approach developed in this work provides us with a path to create low-κ biodegradable nanomaterials from natural polyphenols by weakening their polarizability and introducing high mesoporosity into the structure.

Received 24th February 2021
Accepted 29th April 2021

DOI: 10.1039/d1ra01513c

rsc.li/rsc-advances

Open Access Article. Published on 06 May 2021. Downloaded on 1/13/2026 8:12:45 PM.
This article is licensed under a Creative Commons Attribution-NonCommercial 3.0 Unported Licence.

Introduction

Biodegradable, abundant natural macromolecules and polymers have the ability to reduce the environmental footprint of electronic devices, enabling technologies to interact with nature without leaving long half-life toxic pollutants. They offer a path to mitigate the growth of electronic waste (e-waste) and address the growing demand for flexible electronics.[1–4] Biomass polymers can act as a natural bridge between electronic and soft materials for conducting, semiconducting, and dielectric substrates and offer a vast chemical design space for tunability of electronic, mechanical, and transient properties.[5–8] The tunability of natural soft materials' intrinsic properties is beneficial for the development of complex biodegradable electronics, which have a major impact on the biomedical field, especially in basic research, therapeutics, advanced health monitoring, and drug delivery.[9,10] For such transience devices, numerous biodegradable natural materials have been explored and exhibit practicable electronic properties as substrates, dielectrics, and semiconductors.[5,11–14] However, to overcome their challenges in device compatibility and processing, materials design approaches to natural degradable materials for electronic components, particularly use in semiconductors, electrodes, and dielectrics are required.

Among a wide variety of biodegradable materials and engineered processing methods, natural polymers such as cellulose, lignin, and sugars like glucose and lactose are widely research as promising biodegradable dielectrics.[5,12–14] However, their bulk form exhibits high dielectric constants (κ), ranging from 6.5 to 17.[12–14] With continuous scaling down of field-effect transistors (FETs), the demand for low-κ dielectric materials have grown with the increased need in faster integrated-circuits (ICs). Increasing transistor speed, reducing transistor size, and packing more transistors onto a single chip improve the ICs performance.[15,16] For FETs, biodegradable dielectric with low-dielectric constant (low-κ) is desired to obtain a lower capacitance per area, thereby enabling lower operation voltage and reducing power consumption.[5] Capacitance per area is directly

Nanoscience Department, Joint School of Nanoscience and Nanoengineering, University of North Carolina at Greensboro, NC, 27401, USA. E-mail: hprathna@uncg.edu

† Electronic supplementary information (ESI) available: Additional characterization data (TGA, BET isotherm, and SEM cross-sections of thin film devices) are available. See DOI: 10.1039/d1ra01513c

© 2021 The Author(s). Published by the Royal Society of Chemistry

Open Access Article. Published on 06 May 2021. Downloaded on 1/13/2026 8:12:45 PM.
This article is licensed under a Creative Commons Attribution-NonCommercial 3.0 Unported Licence.

proportional to κ and inversely proportional to the insulator thickness of a defect-free film. Thus, intrinsic material properties and processing methods are essential to select a proper dielectric material. In order to use in capacitors and FETs, natural dielectric materials should exhibit polarizable properties by an electric field, as κ depends on the number of polarizable groups in a material and density of the material.[5] A low-κ dielectric materials should possess weak polarization when subjected to an externally applied electric field whereas high-κ materials should exhibit strong polarizable properties.

One way to design low-κ dielectric materials is to choose materials with chemical bonds of lower polarizability than Si–O. However, most natural polymers are rich in free hydroxyl groups, contributing to high polarity, resulting in high-κ values. Thus, to design low-κ biodegradable dielectric materials from biomass products, either it is necessary to select natural polymers with virtually non-polar bonds such as C–C or C–H or modify hydroxyl groups to weaken the polarity or create a highly porous structure that can result in lower effective κ's, contributing the κ of the air, which is equal to unity. By introducing porosity, also one can manage to increase the free volume and as a result it decreases the density of a material.

Polyphenols serve as versatile building blocks for the preparation of various functional materials, including porous structures by coordinating to metal ions and tailored polarizable substrates by functionalization of hydroxyl groups with non-polar moieties. Owing to these fascinating structural processability and properties, natural polyphenols show the potential of utilizing as versatile platforms for designing environmentally benign engineered dielectric soft materials and surface functionalized substrates. They can also circumvent the need to use complex architectures and patterns to achieve desired properties for electronic devices due to their high-density functionality and selective chemical reactivity. Besides polyphenols' research advancements as capsules, antibacterial and antioxidant films, micro/nanostructures, membranes, components in FETs and energy storage materials, hydrogels, and cell encapsulants,[17–32] a very little research has been conducted on exploring polyphenols as dielectric platforms to use in ICs.[33]

To develop polyphenol-based low-κ dielectric materials, it is necessary to: (1) weaken the polarity by modifying the hydroxyl functionality, (2) introduce porosity into the structure, (3) impart adequate thermal, mechanical, and electrical characteristics, and (4) improve compatibility with the inorganic counterparts of the interconnect structure. Complying with these prerequisites, herein we create a highly nanoporous biodegradable low-κ dielectric nanomaterial from natural tannic acid. Its five pyrogallol and five catechol groups provide multiple bonding sites with diverse interactions, including hydrogen bonds, ionic bonds, coordination bonds, and hydrophobic interactions as well as rich in oxygen sites for selective metal ion binding.[17,18,25–28] In our studies, the porous and robust framework is introduced by randomly functionalizing tannic acid's hydroxyl group (pyrogallol units) with silica network ($SiO_{1.5}$) followed by sol–gel polymerization to produce spherical nanoparticles. The dielectric properties of nanoparticles are reported by fabricating thin film capacitors. The design approach developed in this work to create low-κ biodegradable dielectric nanomaterials can be broadly applied to other types of polyphenols to produce low-κ dielectric natural soft materials on a larger scale. Despite the utilization of tannic acid in components of FETs and energy storage devices,[20–22,24,34] this work is the first demonstration of creating nanoporous low-κ dielectric nanomaterials from tannic acid.

Results and discussion

In this work, base-catalyzed sol–gel process[35] is applied to create nanoporous tannic acid nanoparticles (TA-NPs). Tannic acid's pyrogallol units can be easily modified with an alkyl halide silane precursor to introduce sol–gel reactive sites. The chemistry of making TA-NPs is depicted in Scheme 1. Starting from the silane precursor of tannic acid, nanoporous particles with silsesquioxane core structure of tannic acid was prepared by augmenting a sol–gel polymerization method.[35] The synthesis, particle composition, thermal stability, and morphology analysis were performed. The thin film capacitors were fabricated to evaluate dielectric properties of biodegradable nanoparticles and compared with the dielectric properties of tannic acid, tannic acid-silane, and other literature published biodegradable natural polymers, such as cellulose, glucose, and lactose.

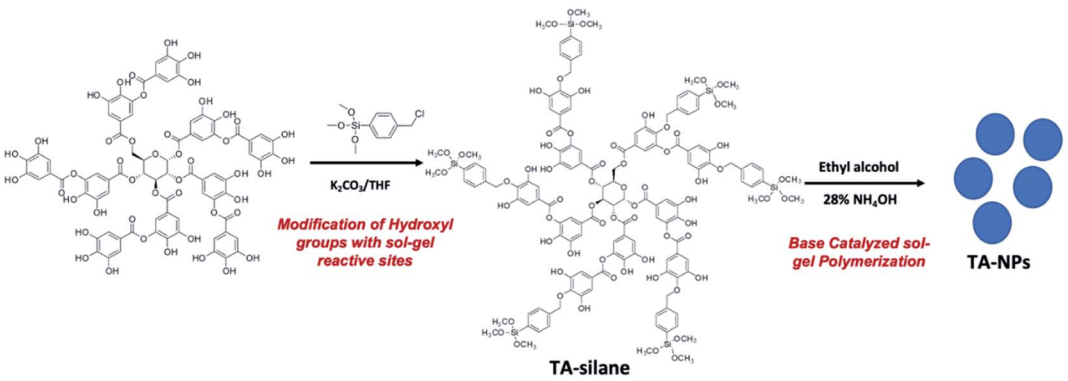

Scheme 1 Chemistry of making nanoporous tannic acid derived nanoparticles (TA-NPs).

Open Access Article. Published on 06 May 2021. Downloaded on 1/13/2026 8:12:45 PM.
This article is licensed under a Creative Commons Attribution-NonCommercial 3.0 Unported Licence.

TA-silane and TA-NPs syntheses and composition analysis

The sol–gel reactive sites were introduced randomly into the tannic acid backbone upon alkylating hydroxyl groups of pyrogallol units with the organosilane precursor using Williamson ether synthesis (Scheme 1). The crude product, tannic acid-silane precursor, (TA-silane) collected by concentrating under vacuum was purified by washing with ethanol followed by deionized water to remove unreacted tannic acid and other products. The FTIR analysis was conducted to confirm the successful incorporation of silane units into the tannic acid structure. As depicted in Fig. 1(a), the FTIR spectrum of TA-silane shows a weak broadening in the range of 3000–3500 cm^{-1}, confirming the modification of hydroxyl groups with silane units. The presence of characteristics bands for Si–O (1120–1025 cm^{-1}) and Si–C (1207 cm^{-1}) further confirms the chemical attachment of silane moieties. The ester carbonyls and aromatic C–C stretching vibrations are observed at 1692 and 1602–1511 cm^{-1}, respectively, confirming the intact structure of tannic acid. The shift in the carbonyl stretching of TA-silane from 1708 cm^{-1} to 1691 cm^{-1} compared to tannic acid also evidences the successful incorporation of alkoxy silane units into the tannic acid structure.

The UV-vis absorption spectrum collected for TA-silane in ethanol is depicted in Fig. 1(b) along with the UV-vis absorption traces of tannic acid and TA-NPs. In general, the tannic acid's absorption spectrum exhibits two absorption maxima at 212 nm and 277 nm with a weak shoulder peak at 240 nm. In comparison to tannic acid absorption, in the TA-silane absorption spectrum, the maximum absorption at 212 nm is disappeared. It also exhibits a growth in the absorption peak at 246 nm, which is ~6 nm red shifted compared to the shoulder peak of tannic acid at 240 nm. While the absorption at 277 nm was less pronounced compared to that of in tannic acid, the additional absorption peak at 344 nm in TA-silane confirms the functionalization of pyrogallol hydroxy groups with benzyl units of organoalkoxy silanes.

The elemental composition analysis along with the XPS survey spectrum of TA-silane depicted in Fig. 2(a) confirms the incorporation of silane units without disrupting the tannic acid glucose core structure. The atomic ratio between Si^{4+} to tannic acid is found to be 6 : 1, indexing the TA-silane empirical formula to $C_{136}H_{136}O_{64}Si_6$. Fig. 2(b)–(d) shows the binding energy spectra for C 1s, O 1s, and Si 2p, respectively. As shown in Fig. 2(b), the presence of well-resolved three characteristics

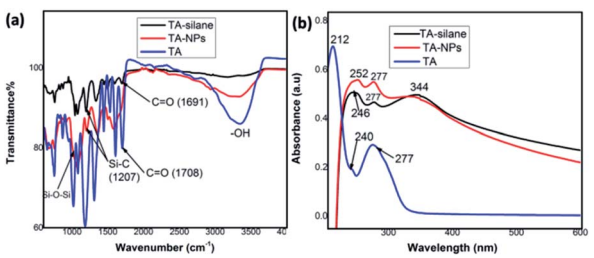

Fig. 1 (a) FTIR spectra and (b) UV-visible spectra of tannic acid (TA), TA-silane, and TA-NPs.

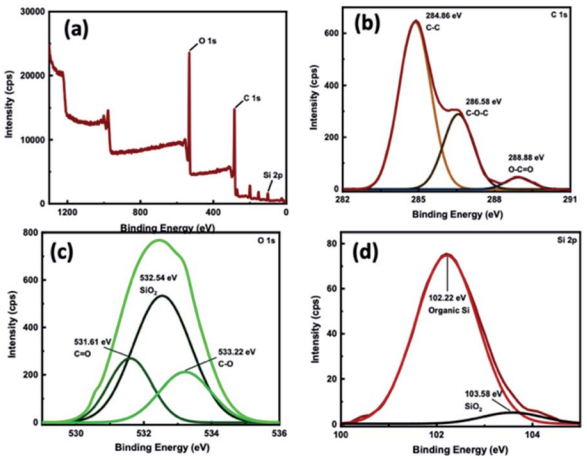

Fig. 2 (a) XPS survey spectrum and binding energy spectra of TA-silane for: (b) C 1s, (c) O 1s, and (d) Si 2p.

binding energy peaks for C 1s at 284.86 eV, 286.58 eV, and 288.88 eV, which correspond to C–C, C–O–C, and O–C=O bonding, confirms the modified tannic acid structure. In the O 1s spectrum in Fig. 2(c), C=O, Si–O, and C–O bonds are confirmed from a poorly resolved broad peak with two shoulder peaks at 531.61, 532.54, and 533.22 eV. The FWHM is 4.29 eV, which further supports the oxygen chemical bonding state of O^{2-}. The binding energies of 531.61 eV and 533.22 eV, which correspond to sp^2 C=O and sp^3 C–O confirm the presence of tannic acid core. The binding energy spectrum of Si 2p, depicted in Fig. 2(d), exhibits one major peak at 102.22 eV along with a weakly resolved shoulder peak at 103.58 eV, which are characteristic to the binding energy for Si–C (organic) and Si–O, respectively, confirming alkoxy silyl units.

Utilizing the previous developed modified Stöber method by our group,[35] TA-NPs were prepared from the base-catalysed direct hydrolysis and condensation of the TA-silane with absence of silica sols as nucleation seeds. In a typical procedure, the silane precursor was added slowly dropwise into a solution of 28% NH_4OH in an anhydrous ethanol. The drop-wise addition is needed to maintain the homogeneity of the particles' formation. The addition of precursors plays a crucial role in maintaining the uniformity of the size and shape of nanoparticles. After 24 hours of reaction time, particles were collected by centrifugation and repeated washing with water and ethanol to yield a brownish solid. A series of controlled experiments were conducted to adjust the reaction parameters, such as base concentration, solvent volume, and reaction time.

The effect of base concentration on the shape and size of the nanoparticles were also investigated by varying the base concentration with respect to the TA-silane precursor. Table 1 summarizes the particle size distribution with respect to the three different base concentrations. The lowest base concentration (8.20 mmol) results considerably uniform spherical particles with the average size of 150 nm. The highest base concentration is also yielded a mix of smaller particles with sizes, ranging from 50–300 nm and larger particles with a wider size distribution from 500 nm to up to ~1 μm. The particles

© 2021 The Author(s). Published by the Royal Society of Chemistry

Open Access Article. Published on 06 May 2021. Downloaded on 1/13/2026 8:12:45 PM.
This article is licensed under a Creative Commons Attribution-NonCommercial 3.0 Unported Licence.

Table 1 The effect of base concentration on particles size and shape

Trail #	28% NH_4OH (mmol)	Shape and dimension
1	8.20	Spherical raspberry-like particles; size distribution: 50–300 nm; average size −150 nm
2	16.40	Spherical, raspberry-like particles; size distribution: 100–500 nm; average size −300 nm
3	32.80	Oval and spherical shape particles; size distribution ranged from 50 nm–1 μm

formed with respect to middle base concentration also exhibit a wider size distribution in the range of 100 nm to 500 nm with a few larger particles in >500 nm <1 μm size range. The base concentration dependent studies suggest that there is no significant effect of the base concentration range that we selected on the particle size distribution. However, 8.20 mmol of base amount yields rather uniform particle size distribution with a considerably smaller size range compared to two higher base concentrations.

The structural composition of TA-NPs is characterized by FTIR, UV-vis, and XPS analysis. The respective FTIR spectrum shown in Fig. 1(a) confirms the presence of characteristics bands for Si–O–Si (1120–1025 cm^{-1}) and Si–C (1376–1317 cm^{-1}) upon the base-catalysed hydrolysis and condensation. The existence of Si–O–Si bonds evidence the formation of silsesquioxane network. The aromatic C=C, ester carbonyl (C=O), and O–H stretching vibrations are observed at 1589, 1693, and 3590 cm^{-1} respectively. The hydroxyl stretching at 3590 cm^{-1} is an indicative of partially condensed residual Si–OH groups, compared to the weak broader peak at 3000–3500 cm^{-1} in TA-silane precursor. The UV-visible spectrum of TA-NPs collected by dispersing ethanol is depicted in Fig. 1(b) and follows the similar characteristics peaks as of TA-silane, evidencing that the tannic acid core structure and silane-ether linkages between silane units and tannic acid are intact.

The elemental composition obtained from the XPS survey analysis confirms the partial hydrolysis and condensation of alkoxy group, yielding silsesquioxane network with suggested empirical formula of $C_{125}H_{109}O_{64}Si_6$. The XPS survey graph and binding energy graphs, depicted in Fig. 3, further reveal the elemental composition, chemical bonding type, and chemical environments of modified tannic acid within the TA-NP's core structure. The binding energies for C 1s and O 1s spectra follow the same trend as the TA-silane precursor, confirming the intact tannic acid core structure. The binding energy spectrum for Si 2p exhibits a slight peak shift with broadening for Si–C bonding environment to higher binding energy, confirming the changes in the chemical environment due to the formation of Si–O–Si network.

In order to utilize TA-NPs in biodegradable dielectrics, they need to possess adequate thermal stability. Therefore, we investigated the thermal stabilities of TA-NPs and the silane precursor using thermogravimetric analysis (TGA). The TGA graphs (Fig. S1†) reveal that first significant weight loss for both TA-NPs and TA-silane take place at 350 °C, suggesting that nanoparticles and silane precursor are thermally stable up to 350 °C. Compared to the TA-silane's TGA curve, TA-NPs exhibits multiple small weight losses, evidencing the degradation of partially hydrolysed alkoxy groups during the polymerization process. Comparing to the thermal stability of tannic acid, which is 240 °C,[36] functionalized tannic acid with silane units and TA-NPs exhibit better thermal stability due to the introduction of silane units and silsesquioxane network into the tannic acid structure.

Morphology and porosity analysis of TA-NPs

Morphologies of TA-NPs prepared by varying the base concentrations were visualized using SEM and are depicted in Fig. 4. At lower base concentration, particles are uniform and spherical in shape with a raspberry-like surface morphology (Fig. 4(a)). The particles formed at the medium base concentration are also somewhat spherical but average particle diameter is larger than the lowest and the highest base concentration (Fig. 4(b)). At the highest base concentration, both significantly larger and somewhat oval in shape particles were formed and exhibit also a raspberry-like surface. TEM images of TA-NPs in Fig. 5(a) reveal the condensed silsesquioxane core structure (dark core) and interparticle large pores, creating mesoporous microstructures. The selective area electron diffraction (SAED) pattern (Fig. 5(b)) evidences the crystallinity of particles, confirming the packing of phenyl rings of tannic acid in the framework. The pore size distribution and pore volume, obtained from the N_2-adsorption isotherm using Barrett–Joyner–Halenda (BJH) analysis, particles are mesoporous, having average diameter of pores ranged from 19 to 23 nm and pore volume of 0.032 $cm^3\ g^{-1}$. The TEM images shown in Fig. 5(c) and (d) further supports the mesoporous structures within and in-between particles along

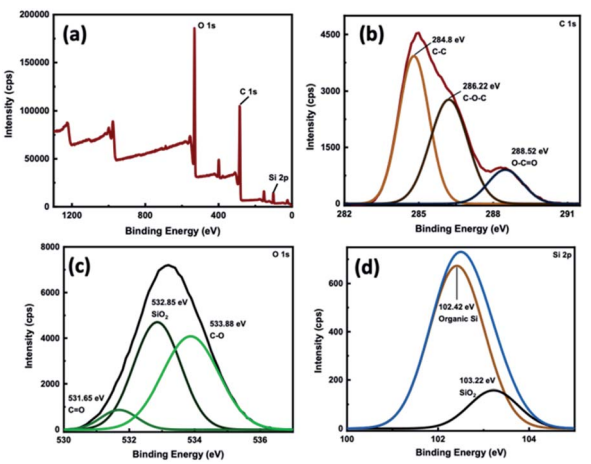

Fig. 3 (a) XPS survey spectrum and binding energy spectra of TA-NPs for: (b) C 1s, (c) O 1s, and (d) Si 2p.

Open Access Article. Published on 06 May 2021. Downloaded on 1/13/2026 8:12:45 PM.
This article is licensed under a Creative Commons Attribution-NonCommercial 3.0 Unported Licence.

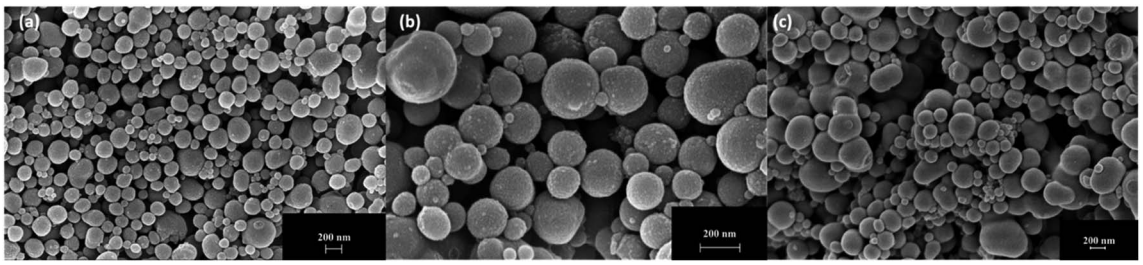

Fig. 4 SEM images of TA-NPs prepared with respect to different base concentrations; (a) At 8.20 mmol, (b) 16.40 mmol, and (c) 32.80 mmol.

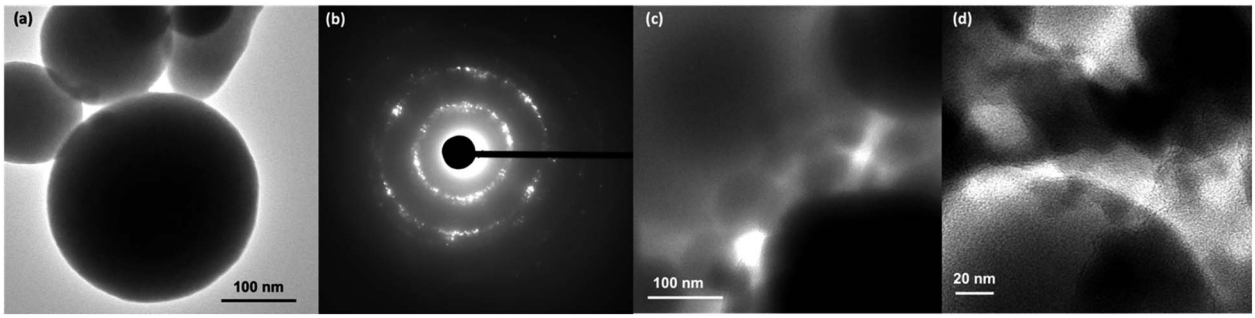

Fig. 5 (a) A TEM image of TA-NPs with large interparticle pores; (b) The SAED pattern of TA-NPs evidencing crystallinity; and (c) and (d) TEM images of TA-NPs showing mesoporous structure.

with a textural nanoporosity within the particle's framework. The isotherms of TA-NPs (Fig. S2†) exhibit hysteresis between adsorption/desorption curves that resemble isotherm type IV, indicating that the capillary condensation takes place, resembling to mesoporous materials.

Evaluation of dielectric properties of tannic acid, TA-silane and TA-NPs

We hypothesize that creating biodegradable porous framework with silsesquioxane structure may lower the dielectric constant of tannic acid, yielding low-κ bio-based nanomaterials. To test our hypothesis, dielectric properties of tannic acid, TA-silane, and TA-NPs were analyzed and compared each other by fabricating thin film capacitors from material. The dielectric constants were calculated from the test capacitor devices, having the active device area of 4.75 cm^2 and film thickness ranged from 850 nm to 880 nm (Fig. S3†). The detailed experimental procedure for the device fabrication is described in the Experimental section. A representative device schematic is shown in the inset of Fig. 6. The dielectric constants were calculated using the eqn (1). Repetitive capacitance was measured for each sample at more than 8 to 12 points with high consistency, confirming the film uniformity and continuity throughout the active area of the thin films. Fig. 6 represents comparison graphs of average dielectric constants calculated for tannic acid, TA-silane, and TA-NPs. The average dielectric constant for tannic acid was found to be 2.98 $\pm$ 0.02, which is significantly lower than the dielectric constants of cellulose, glucose, and lactose, which range from 6.5 to 17.[5,12–14] Also, this is the first time of reporting the dielectric constant for tannic acid. Comparing to tannic acid's κ, TA-silane yields a slightly lower κ ($\kappa = 2.84 \pm 0.02$). As we expected, the κ of TA-NPs is much lower ($\kappa = 2.69 \pm 0.02$). Previously, we have demonstrated that the silsesquioxane framework can result mesoporous low-κ polymeric nanomaterials.[35] Similarly, in this work, the silsesquioxane framework and mesoporosity have affected to lower the dielectric constant of tannic acid by creating porous silsesquioxane framework of tannic acid.

Experimental

Materials

Tannic acid ($C_{76}H_{52}O_{46}$; molar mass = 1701.19 g mol^{-1}), potassium carbonate, tetrahydrofuran (THF), 28% ammonium hydroxide, and anhydrous ethanol (200 proof) were obtained from Sigma-Aldrich. *para*-(Chloromethyl) phenylethyl

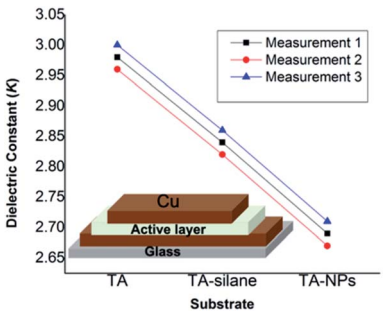

Fig. 6 The comparison graph for average dielectric constants calculated for tannic acid, TA-silane, and TA-NPs; inset – a schematic diagram of the capacitance device.

© 2021 The Author(s). Published by the Royal Society of Chemistry

Open Access Article. Published on 06 May 2021. Downloaded on 1/13/2026 8:12:45 PM.
This article is licensed under a Creative Commons Attribution-NonCommercial 3.0 Unported Licence.

trimethoxy silane were obtained from Gelest Inc. All chemicals were used as received.

Characterization

The chemical composition and functional groups were analyzed using Fourier transform infrared spectroscopy (FTIR-Varian 670-IR spectrometer). The morphology and the particle size of nanostructures were analysed using transmission electron microscopy (TEM Carl Zeiss Libra 120 and JEOL2100PLUS HR-TEM with STEM/EDS) at 120 keV and 200 keV, respectively, and scanning electron microscopy (Zeiss Auriga FIB/FESEM). The thermal stability of microstructures was analyzed using the thermogravimetric analyzer Q500. Samples were heated up to 700 °C at the increment of 10°C min^{-1} in nitrogen gas flow. The elemental composition was obtained from an elemental composition analyzer and X-ray photon spectroscopy (XPS-Escalab Xi^{+}-Thermo Scientific) respectively. Brunner–Emmett–Teller (BET) method was used to determine the pore size and the pore volume density distribution of the products. The UV-visible spectra were obtained using the UV-visible spectrometer (Varian Cary 6000i). E-beam evaporation (Kurt Lesker PVD 75 e-beam evaporator) was used to deposit the Cu layer with a thickness of 100 nm. Thin films were prepared by spin coating the colloidal solution of nanomaterials and the silane precursor in ethanol onto ozone/UV treated substrates of either quartz plates or ITO coated glass substrates. Ozone/UV treatment was performed using the Bio Force UV/Ozone Pro Cleaner.

Synthesis of sol–gel reactive site functionalized tannic acid (TA-silane)

To a 100 mL round-bottom flask, tannic acid (500 mg, 0.294 mmol) and potassium carbonate (203 mg, 1.47 mmol) were added with tetrahydrofuran (50 mL). The beige (greyish yellow) colour mixture was stirred for 2 hours under ambient conditions. Then *para*-(chloromethyl)-phenylethyltrimethoxy silane (0.318 mL, 1.47 mmol) was added to the stirring mixture and the colour was turning to brown slowly. Then it was stirred for 24 hours under ambient conditions. The resulted suspension was concentrated in a rotary evaporator while maintaining the temperature of the water bath at 54 °C. The brown, dry, crude product collected in this manner was washed with hexane (~40 mL) followed by deionized water. The precipitate was collected and dried for 24 hours to yield brown colour solid (600 mg, 80%). FTIR stretching (cm^{-1}): 1025 (Si–O), 1207 (Si–C), 1673 (aromatic C=C), and 1712 (ester C=O); elemental analysis (from XPS) for the empirical formula of $C_{136}H_{136}O_{64}Si_6$: % experimental – C (61.24), O (33.54), Si (5.22); calculated – C (55.13), O (34.56), Si (5.69).

Synthesis of tannic acid-silsesquioxane nanostructures by sol–gel method

In a typical procedure, to a 100 mL round-bottom flask, ethyl alcohol (140 proof, 6.0 mL) and 28% ammonium hydroxide solution (2 mL, or 1.0 mL or 0.5 mL) were added with a stir bar and mixed for 10 min. A solution of TA-silane (98.0 mg) in ethyl alcohol (140 proof, 4.0 mL) was slowly added to the reaction flask and stirred 24 h under room temperature. Particles were separated by centrifuging the brownish cloudy suspension at the rate of 10 000 rpm for 30 minutes. Particles were washed multiple times with ethanol. Particles obtained by final washing were dried for 24 h, yielding a brownish white solid (50 mg, (w/w) yield ~50%). FTIR stretching (cm^{-1}): 1120–1025 cm^{-1} (Si–O–Si), 1376–1317 cm^{-1} (Si–C), 1589 cm^{-1} (aromatic C=C), and 1693 cm^{-1} (ester C=O); elemental analysis (from XPS) for the empirical formula of $C_{125}H_{109}O_{64}Si_6$ – C (58.2.24), O (35.40), Si (6.76).

N_2 adsorption–desorption isotherms

Brunner–Emmett–Teller (BET) method was used to determine the pore size and the pore volume distribution of the nanomaterials. In order to measure pore volume distribution accurately, it is necessary to remove surface adsorbed and pore occupied guest molecules such as residual solvent molecules (ethanol and water), prior to degassing the samples. For this purpose, the samples obtained were activated for BET analysis by soaking the samples in chloroform for three consecutive days by replacing with fresh chloroform for every 6 hours. Here we use dry chloroform instead THF, as chloroform may have minimal interactions with silsesquioxane network compared to oxygen rich THF, which can occupy the pores. Before measurements, the samples were dried under vacuum at 80 °C for 3 hours followed by degassing of samples at 150 °C for 12 hours. In BET analysis, the surface area is calculated based on the equation obtained from adsorption isotherm in the relative pressure range of $P/P_0 = 0.07$–0.3. The information about the pore size distribution is derived from N_2 desorption isotherms using Barrett–Joyner–Halenda (BJH) plots. Further, the total volume of the product per gram is determined from the amount of N_2 adsorbed at $P/P_0 = 1$.

Device fabrication for dielectric constant measurements

The glass coverslips were cleaned by sonicating in isopropanol for 15 min followed by the sonication in DI water for 15 min. Then the substrate was dried with the nitrogen gun. Once dried, the coverslips were subjected to ozone cleaning for 60 min. The substrates were then placed in a mask made from the poly (lactic acid) resin materials and sandwiched before coating copper (~100 nm thick) using physical vapor deposition (PVD). This layer acts as the first electrode of the capacitor. Then 1 mg of sample in 500 μL 70% ethanol was immediately spin-coated on the copper-coated substrate at a spin rate of 1000 rpm for the 60 s and dried at 100 °C for 15 minutes. The second electrode of the copper layer was immediately deposited using PVD. The substrate was sandwiched in the PLA mask and 100 nm of copper is deposited at a 90° rotation to the first layer. Capacitance was then measured with a CM9610A between the electrodes that form a capacitor area of 4.75 cm^2. Using the following eqn (1), the dielectric constant (k) of nanomaterials thin films was calculated:

$$k = \frac{tC_p}{Sk_0} \quad (1)$$

Open Access Article. Published on 06 May 2021. Downloaded on 1/13/2026 8:12:45 PM.
This article is licensed under a Creative Commons Attribution-NonCommercial 3.0 Unported Licence.

where, t is the thickness of the sample, S is the area of the electrode, and k_0 is equal to 8.85×10^{-12} F m^{-1}.

Thickness measurement

The thickness of the dielectric layer was measured by viewing the broken side of a device under SEM. After the measurements of capacitance, devices were broken using liquid nitrogen and the broken side was mounted on an SEM stub. The stage was rotated by 60° and the tilt angle was kept at 30°. The tilt correction was done for imaging the layers using the back-scattered electron detector. The thickness of the thin films was consistent throughout each sample and the range of the thickness of the films was within the range of 850 to 880 nm (Fig. S3†). Average film thicknesses were 879.6 nm, 870.9 nm, and 859.0 nm, for tannic acid, TA-silane, and TA-NPs, respectively.

Conclusions

The work describes herein is the first demonstration of creating low-κ dielectric nanomaterials (TA-NPs) from tannic acid by modifying tannic acid's pyrogallol units with alkoxy silane moieties followed by introducing silsesquioxane framework *via* base-catalysed sol–gel polymerization. Controlling the size and shape of TA-NPs have attempted by varying the molar ratio between the silane precursor and the base. The lowest base concentration has yielded spherical raspberry-like particles with an average diameter of 150 nm. The porosity distribution, confirmed by the BET analysis reveals that nanoparticles are mesoporous in nature with average pore diameter, ranging from 19 to 23 nm and pore volume of 0.032 cm^3 g^{-1}. Weakening the polarizability and introducing a porous framework into the tannic acid structure allow us to lower the dielectric properties of tannic acid from its bulk κ of 2.98 to 2.69 for the nanomaterials. Thus, the unique chemical design approach developed in this work offers a novel and versatile path to create novel low-κ biodegradable nanomaterials from natural polyphenols. Our future work will focus on fabricating patterned low-κ dielectric platforms using TA-NPs and utilize them in organic field effect transistors.

Author contributions

This manuscript was written by the corresponding author through the contribution of all authors. Sujoy Saha has made 60% contribution to this research work and recognized as the first author. Sheeba Dawood made 20% contribution as the second author and remaining two co-authors, Pravalika Butreddy and Gayani Pathiraja made equal contributions as third and fourth authors, respectively.

Conflicts of interest

There are no conflicts to declare.

Acknowledgements

This work is performed at the Joint School of Nanoscience and Nanoengineering, a member of the South-eastern Nanotechnology Infrastructure Corridor (SENIC) and National Nanotechnology Coordinated Infrastructure (NNCI), supported by the NSF (Grant ECCS-1542174). Financial support for this work is provided, in part, from the Joint School of Nanoscience and Nanoengineering and the Office of Research, University of North Carolina at Greensboro. Authors also acknowledge the DOD HBCU/MSI instrumentation award (Contract #: W911NF1910522) to acquire HR-TEM (JEOL 2100PLUS) with STEM/EDS capability.

References

1 M. Irimia-Vladu, E. D. Głowacki, G. Voss, S. Bauer and N. S. Sariciftci, *Mater. Today*, 2012, **15**, 340–346.
2 C. P. Baldé, F. Wang, R. Kuehr and J. Huisman, *The Global E-waste Monitor 2014*, United Nations University, IAS – SCYCLE, Bonn, 2015.
3 R. Afroz, M. M. Masud, R. Akhtar and J. B. Duasa, *J. Cleaner Prod.*, 2013, **52**, 185–193.
4 N. Singh, J. Li and X. Zeng, *Waste Manag.*, 2016, **57**, 187–197.
5 V. R. Feig, H. Tran and Z. Bao, *ACS Cent. Sci.*, 2018, **4**, 337–348.
6 U. Zschieschang, T. Yamamoto, K. Takimiya, H. Kuwabara, M. Ikeda, T. Sekitani, T. Someya and H. Klauk, *Adv. Mater.*, 2011, **23**, 654–658.
7 B. Peng, X. Ren, Z. Wang, X. Wang, R. C. Roberts and P. K. L. Chan, *Sci. Rep.*, 2015, **4**, 6430.
8 L. Leonat, M. S. White, E. D. Głowacki, M. C. Scharber, T. Zillger, J. Rühling, A. Hübler and N. S. Sariciftci, *J. Phys. Chem. C*, 2014, **118**, 16813–16817.
9 L. S. Nair and C. T. Laurencin, *Prog. Polym. Sci.*, 2007, **32**, 762–798.
10 K. E. Uhrich, S. M. Cannizzaro, R. S. Langer and K. M. Shakesheff, *Chem. Rev.*, 1999, **99**, 3181–3198.
11 S.-W. Hwang, C. H. Lee, H. Cheng, J.-W. Jeong, S.-K. Kang, J.-H. Kim, J. Shin, J. Yang, Z. Liu, G. A. Ameer, Y. Huang and J. A. Rogers, *Nano Lett.*, 2015, **15**, 2801–2808.
12 K. Deshmukh, M. B. Ahamed, R. R. Deshmukh, S. K. K. Pasha, K. K. Sadasivuni, A. R. Polu, D. Ponnamma, M. A.-A. AlMaadeed and K. Chidambaram, *J. Mater. Sci.: Mater. Electron.*, 2017, **28**, 973–986.
13 X. Zeng, L. Deng, Y. Yao, R. Sun, J. Xu and C.-P. Wong, *J. Mater. Chem. C*, 2016, **4**, 6037–6044.
14 E. Jayamani, S. Hamdan, M. R. Rahman and M. K. Bin Bakri, *Procedia Eng.*, 2014, **97**, 536–544.
15 K. Maex, M. R. Baklanov, D. Shamiryan, F. Lacopi, S. H. Brongersma and Z. S. Yanovitskaya, *J. Appl. Phys.*, 2003, **93**, 8793–8841.
16 T. Gupta, in *Copper Interconnect Technology*, Springer, New York, 2009, pp. 67–110.
17 J. Yang, M. A. Cohen Stuart and M. Kamperman, *Chem. Soc. Rev.*, 2014, **43**, 8271–8298.

© 2021 The Author(s). Published by the Royal Society of Chemistry

Open Access Article. Published on 06 May 2021. Downloaded on 1/13/2026 8:12:45 PM.
This article is licensed under a Creative Commons Attribution-NonCommercial 3.0 Unported Licence.

18 I. Erel-Unal and S. A. Sukhishvili, *Macromolecules*, 2008, **41**, 8737–8744.
19 P. R. Pudasaini, J. H. Noh, A. T. Wong, O. S. Ovchinnikova, A. V. Haglund, S. Dai, T. Z. Ward, D. Mandrus and P. D. Rack, *Adv. Funct. Mater.*, 2016, **26**, 2820–2825.
20 S. Bubel, M. S. Menyo, T. E. Mates, J. H. Waite and M. L. Chabinyc, *Adv. Mater.*, 2015, **27**, 3331–3335.
21 Y. A. Lee, J. Lee, D. W. Kim, C.-Y. Yoo, S. H. Park, J. J. Yoo, S. Kim, B. Kim, W. K. Cho and H. Yoon, *J. Mater. Chem. A*, 2017, **5**, 25368–25377.
22 J. Y. Oh, Y. Jung, Y. S. Cho, J. Choi, J. H. Youk, N. Fechler, S. J. Yang and C. R. Park, *ChemSusChem*, 2017, **10**, 1675–1682.
23 Y. Zhang, J.-J. Yuan, Y.-Z. Song, X. Yin, C.-C. Sun, L.-P. Zhu and B.-K. Zhu, *Electrochim. Acta*, 2018, **275**, 25–31.
24 C. Wu, T. Li, C. Liao, L. Li and J. Yang, *J. Mater. Chem. A*, 2017, **5**, 12782–12786.
25 H. Zhou, X. Sun, L. Zhang, P. Zhang, J. Li and Y.-N. Liu, *Langmuir*, 2012, **28**, 14553–14561.
26 M. A. Rahim, H. Ejima, K. L. Cho, K. Kempe, M. Müllner, J. P. Best and F. Caruso, *Chem. Mater.*, 2014, **26**, 1645–1653.
27 C. Das, S. Chatterjee, G. Kumaraswamy and K. Krishnamoorthy, *J. Phys. Chem. C*, 2017, **121**, 3270–3278.
28 C. Das and K. Krishnamoorthy, *ACS Appl. Mater. Interfaces*, 2016, **8**, 29504–29510.
29 T. Shutava, M. Prouty, D. Kommireddy and Y. Lvov, *Macromolecules*, 2005, **38**, 2850–2858.
30 H. Fan, L. Wang, X. Feng, Y. Bu, D. Wu and Z. Jin, *Macromolecules*, 2017, **50**, 666–676.
31 Z. Xu, H. Ye, H. Li, Y. Xu, C. Wang, J. Yin and H. Zhu, *ACS Omega*, 2017, **2**, 1273–1278.
32 S. Çakar, N. Güy, M. Özacar and F. Fındık, *Electrochim. Acta*, 2016, **209**, 407–422.
33 E. Shin, J. Yoo, G. Yoo, Y.-J. Kim and Y. S. Kim, *Chem. Eng. J.*, 2019, **358**, 170–175.
34 Y.-Z. Song, Y. Zhang, J.-J. Yuan, C.-E. Lin, X. Yin, C.-C. Sun, B. Zhu and L.-P. Zhu, *J. Electroanal. Chem.*, 2018, **808**, 252–258.
35 M. Hawkins, S. Saha, E. Ravindran and H. Rathnayake, *J. Polym. Sci., Part A: Polym. Chem.*, 2019, **57**, 562–571.
36 T. Xia, Y. Wang, B. Wang, Z. Yang, G. Pan, L. Zhang and J. Zhang, *ChemElectroChem*, 2019, **6**, 4765–4772.

© 2021 The Author(s). Published by the Royal Society of Chemistry